Graphene superlattices in strong circularly polarized fields: Chirality, Berry phase, and attosecond dynamics

Hamed Koochaki Kelardeh,[*] Vadym Apalkov,[†] and Mark I. Stockman[‡]
Center for Nano-Optics (CeNO) and Department of Physics and Astronomy, Georgia State University, Atlanta, Georgia 30303, USA
(Received 28 March 2017; published 7 August 2017)

We propose and theoretically explore states of graphene superlattices with relaxed $\mathcal{P}$ and $\mathcal{T}$ symmetries created by strong circularly polarized ultrashort pulses. The conduction-band electron distribution in the reciprocal space forms an interferogram with discontinuities related to topological (Berry) fluxes at the Dirac points. This can be studied using time- and angle-resolved photoemission spectroscopy (TR-ARPES). Our findings hold promise for control and observation of ultrafast electron dynamics in topological solids and may be applied to petahertz-scale information processing.

DOI: 10.1103/PhysRevB.96.075409

I. INTRODUCTION

Topological properties of quantum-mechanical Hilbert space have had pronounced influence on physics as a whole and condensed matter physics in particular [1–4]. Nontrivial topological properties of graphene in the reciprocal **k**-space are due to the presence of nonzero Berry curvature $\Omega(\mathbf{k})$, which is a geometric counterpart of a magnetic field localized at the Dirac points [4,5]. The flux of Ω at the K or K' points is equal to $\pm\pi$, correspondingly. The Berry flux is a topological counterpart of the Ehrenberg-Siday-Bohm-Aharonov (ESBA) phase [6–8] caused by a localized magnetic field. The total flux integrated over all the Dirac points is zero, corresponding to the zero Chern number.

While the Berry phase in the reciprocal space is analogous to the ESBA phase [7] in the real space, there is a fundamental difference in the ways it can be observed. In the real space, an electron wave can diffract around the region containing magnetic flux and, then, interfere with itself exhibiting fringes shifted due to the ESBA phase [8]. In sharp contrast, in the reciprocal space an electron motion in the absence of a magnetic field is deterministic and diffractionless due to the Bloch acceleration theorem [9]. In accord with this theorem, the crystal momentum, $\mathbf{k}_T(t)$, as a function of time t evolves as

$$\mathbf{k}_T(t) = \mathbf{k}_0 + \frac{e}{\hbar c}\mathbf{A}_L(t), \quad \mathbf{A}_L(t) = -c\int \mathbf{F}_L(t)dt, \qquad (1)$$

where e is unit charge, $\hbar$ is reduced Planck constant, $\mathbf{F}_L(t)$ is the optical electric field, $\mathbf{A}_L(t)$ is the vector potential, and $\mathbf{k}_0$ is the initial crystal wave vector of the electron. After the pulse ends, the crystal momentum deterministically returns to its original value, $\mathbf{k}_T(t) \to \mathbf{k}_0$, and, consequently, there can be no interference of an electron wave with itself.

To deal with this fundamental problem, we have proposed [10] a self-referenced interferometry in the reciprocal space of graphene. However, because the Berry phase is $\pm\pi$, the corresponding self-referenced interference term carries a double phase, $\pm 2\pi$, which is equivalent to zero and not observable directly. However, one can see an indirect effect of the Berry phase as an extra interference fringe typical for a vortex. Direct observation of the reciprocal space Berry phase is possible by the application of a time-dependent and inhomogeneous magnetic field [5], or by a circular shaking of the lattice [11]. However, such experiments are only possible on quantum lattice models.

Here we propose an approach to directly observe the Berry phase without a magnetic field. The idea is to use a superlattice superimposed on graphene to cause electron diffraction (Bragg reflection) in the reciprocal space. That causes the self-referenced phase to be different from $\pm 2\pi$ and, therefore, to be observable directly by the reciprocal space interferometry. In other terms, the diffraction from the superlattice creates a "which way" quantum-mechanical uncertainty causing interference of the electron wave with itself and making the Berry phase directly visible in discontinuities of the self-referenced interferogram. In a sense, this article differs from our Ref. [10] analogously to how observation of the ESBA phase by electron interferometry [8] differed from the discovery of electron diffraction [12].

We emphasize that we propose to measure the Berry phase in its direct definition as a phase accumulated by an electron while adiabatically moving around a Dirac point. In our article, the phase accumulated by an electron is a combination of the Berry phase and the dynamic phase. This total phase results in a unique interference pattern in the conduction-band population distribution in the reciprocal space, while the presence of the Berry phase results in singularities (discontinuities) in this distribution. Note that in the previously published research [13,14] the Berry phase is not observed directly as the phase due to adiabatic circling around a Dirac point but through a unique angular dependence of the interband matrix elements in graphene related to a specific structure of the electron wave function defined by the crystallographic symmetry.

Specific properties of graphene as constituted from light carbon atoms allows one to neglect the spin-orbit interaction, which is known to be negligibly small ($\sim$1 μeV) in graphene [15,16]. In contrast, in three-dimensional topological insulators, such as Bi_xSb_{1-x}, Bi_2Te_3, Sb_2Te_3, and Bi_2Se_3, whose surface states have gapless relativistic energy dispersion laws similar to graphene [17–24], the spin-orbit interaction is a

[*]hkoochakikelardeh1@student.gsu.edu
[†]vapalkov@gsu.edu
[‡]mstockman@gsu.edu

major factor defining their nontrivial topological properties. Correspondingly, a theory of phenomena at the surfaces in strong chiral fields will be significantly different to necessarily take into account the spin-orbit interaction. There will also be other significant differences related to the presence of the bulk semiconducting bands and surface-bulk mixing. However, the underlying idea of the present article that the strong chiral fields, which compel electrons to move along closed orbits in the reciprocal space acquiring the Berry phase when the Dirac point is inside the orbit, will still lead to interference effects similar to those described in the present article. As it turns out, such a theory for topological insulators is complicated and specific enough to require dedicated publications elsewhere; cf. Ref. [25].

II. MODEL

Assume a graphene monolayer positioned in the xy plane with the radiation incident in the z direction; see inset in Fig. 1. A single-oscillation pulse field is defined by its electric field vector $\mathbf{F}_L = \{F_x, F_y, 0\}$ where

$$F_x(t) = -F_0 e^{-u^2}(1-2u^2), \quad F_y(t) = \pm 2F_0 u e^{-u^2}, \qquad (2)$$

$\pm$ signs correspond to opposite circularities, F_0 is the amplitude, which is related to the pulse power as $P = cF_0^2/4\pi$, c is speed of light, $u = t/\tau$, and $\tau \approx 1$ fs is approximately a quarter optical oscillation period. Assuming a vacuum wavelength of 1.5 μm, the duration of the pulse is $T = 5$ fs.

Experimentally, the processes of energy-momentum relaxation in the photoexcited CB electron population occur during times ranging from ~10–20 fs to ~200–800 fs [26–33] where the shortest, ~10 fs, times are due to ultrafast electron-electron interactions while longer, ~1 ps, times are those of phonon-assisted cooling.

An advantage of ultrafast strong-field processes considered in this article is that the full cycle of optical excitation is completed within a few femtoseconds when the electron relaxation processes do not have enough time to occur. Therefore, the electron relaxation can be neglected. Note that effects described below in this paper have a topological origin and, as characteristic of topological properties, they should be stable with respect to perturbations.

Consequently, the electron dynamics can be considered to be coherent, and one can describe it by time dependent Schrödinger equation (TDSE),

$$i\hbar\partial_t \psi(t) = \hat{H}(t)\psi(t). \qquad (3)$$

Here the Hamiltonian is

$$\hat{H} = \hat{H}_0 + e\mathbf{F}_L(t)\,\mathbf{r} + \Delta(y), \qquad (4)$$

where $\hat{H}_0$ is the field-free Hamiltonian, $\mathbf{r} = \{x, y\}$ is a two-dimensional (2D) radius vector in the plane of graphene, and $\Delta(y) = V_0 \cos(Q_y y)$ is an electrostatic potential of the superlattice, which is periodic in the y direction with period L and amplitude V_0. Here $\mathbf{Q}$ is the reciprocal vector of the supelattice: $\mathbf{Q} = \{0, Q_y, 0\}$ with $Q_y = 2\pi/L$. We used realistic parameters: $L = 10$ nm and $V_0 = 0.05$ eV. The dipole approximation used here is applicable since the unit cell is much smaller than the radiation wavelength and the electron velocities are much smaller than the speed of light.

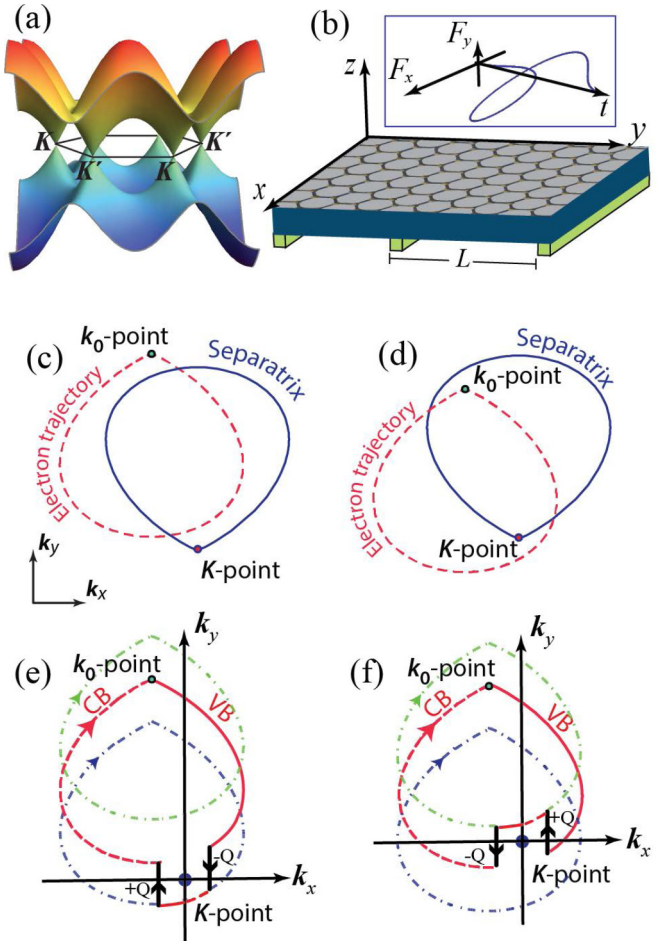

FIG. 1. Real- and reciprocal-space structure of the system and electron trajectories for a single-oscillation circularly polarized ultrashort pulse. (a) Electron dispersion of a graphene monolayer obtained within the tight-binding approximation. Energies of the highest valence band (π band) and the lowest conduction band (π^* band) in the reciprocal space are displayed as functions of wave vector $\mathbf{k} = \{k_x, k_y\}$. The two distinct sets of Dirac points are labeled K and K'. (b) Schematic of the proposed structure. A graphene monolayer is positioned over a superlattice formed by nanowires with period L in the y direction. Inset: Electric field waveform $\mathbf{F}(t) = \{F_x(t), F_y(t)\}$ as a function of time t. (c) An illustration of an electron trajectory (dashed red line) in the reciprocal space, which starts and ends at a $\mathbf{k}_0$ point outside the separatrix and passes close to a K point without circling around it. The separatrix (solid blue line) separates the $\mathbf{k}_0$ points for those trajectoris that circle around the K point and those that do not. (d) The same as in panel (c) but for the $\mathbf{k}_0$ point inside the separatrix. (e) Schematic of the reciprocal space trajectories and transitions caused by the Bragg reflections for the $\mathbf{k}_0$ point outside of the separatrix, corresponding to the case of panel (c). The red line shows an electron trajectory where the solid and dashed segments correspond to the VB and CB, respectively, as indicated. The thin dash-dot green and blue lines are the Bragg-shifted replica of the original trajectory. See other details in the text. (f) The same as in panel (e) but for the $\mathbf{k}_0$ point inside the separatrix, corresponding to the case of panel (d).

We solve the TDSE (3) using a basis of Houston functions [34] as has previously been described [10,35,36]. We consider

graphene at the point of neutrality where the Fermi surface is at the Dirac points.

The field-free electron Hamiltonian, $\hat{H}_0$, is described by the tight-binding model with nearest neighbor hopping. It is convenient to write the TB eigenfunctions in the form of a spinor (describing pseudospin), whose components correspond to the amplitudes on the A and B sublattices, respectively, within the unit cell. Then the resulting Hamiltonian $\hat{H}_0$ in the reciprocal space is a purely off-diagonal 2×2 matrix of the form

$$\hat{H}_0 = \begin{pmatrix} 0 & \gamma f(\mathbf{k}) \\ \gamma f^*(\mathbf{k}) & 0 \end{pmatrix}, \tag{5}$$

where $\gamma \approx -3$ eV is the nearest-neighbor hopping (or transfer) constant, and

$$f(\mathbf{k}) = \exp\left(i\frac{ak_x}{\sqrt{3}}\right) + 2\exp\left(-i\frac{ak_x}{2\sqrt{3}}\right)\cos\left(\frac{ak_y}{2}\right). \tag{6}$$

The eigenvalues of Hamiltonian $\hat{H}_0$ are given by

$$\begin{aligned} &E(\mathbf{k}) \\ &= \pm\gamma|f(\mathbf{k})| \\ &= \pm\gamma\sqrt{1 + 4\cos(ak_y/2)\cos(\sqrt{3}ak_x/2) + 4\cos^2(ak_y/2)}, \end{aligned} \tag{7}$$

where the $+$ and $-$ signs correspond to the VB and CB, respectively. The corresponding wave functions of the CB and VB are

$$\Psi_{\mathbf{k}}^{(c)}(\mathbf{r}) = \frac{e^{i\mathbf{k}\cdot\mathbf{r}}}{\sqrt{2}}\begin{pmatrix} 1 \\ e^{i\varphi_k} \end{pmatrix} = |\mathrm{c},\mathbf{k}\rangle \tag{8}$$

and

$$\Psi_{\mathbf{k}}^{(v)}(\mathbf{r}) = \frac{e^{i\mathbf{k}\cdot\mathbf{r}}}{\sqrt{2}}\begin{pmatrix} -1 \\ e^{i\varphi_k} \end{pmatrix} = |\mathrm{v},\mathbf{k}\rangle, \tag{9}$$

where $f(\mathbf{k}) = |f(\mathbf{k})|e^{i\varphi_k}$. The wave functions, $\Psi_{\mathbf{k}}{}^{(c)}$ and $\Psi_{\mathbf{k}}{}^{(v)}$, have two components corresponding to amplitudes to be on graphene sublattices A and B.

The electric field of the optical pulse generates both interband and intraband electron quantum transitions. The interband transitions, VB $\leftrightarrow$ CB, cause a redistribution of the electron population between different bands. The temporal dynamics for a state with initial crystal momentum $\mathbf{k}_0$ is universally expressed by the Bloch acceleration theorem: the time-dependent wave vector is given by $\mathbf{k}_T(\mathbf{k}_0,t) = \mathbf{k}_0 + e/\hbar\int_{-\infty}^{t}\mathbf{F}_L(t')dt'$. Consequently, the states, which belong to different bands (VB and CB) but have the same initial crystal momentum, $\mathbf{k}_0$, will have the same crystal momentum, $\mathbf{k}_T(\mathbf{k}_0,t)$, at all moments of time t; after the pulse ends, the crystal momentum returns to its initial value $\mathbf{k}_0$. The periodic potential, $\Delta(y)$, couples states within each band with crystal moments $\mathbf{k}$ and $\mathbf{k}' = \mathbf{k} + n\mathbf{Q}$, where $n = \pm1, \pm2, \ldots$ is the order of the Bragg reflection from the underlying periodic array of the metal nanowires.

We use the Houston functions [34]

$$\Phi_{\alpha\mathbf{k}_0}^{(H)}(\mathbf{r},t) = \Psi_{\mathbf{k}_T(\mathbf{k}_0,t)}^{(\alpha)}\exp\left\{-\frac{i}{\hbar}\int_{-\infty}^{t}E_\alpha[\mathbf{k}_T(\mathbf{k}_0,t')]\,dt'\right\} \tag{10}$$

as the basis, where $\alpha = v$ (VB) or $\alpha = c$ (CB). Then the general solution of the time-dependent Schrödinger equation is expressed in the following form:

$$\Psi_{\mathbf{k}_0}(\mathbf{r},t) = \sum_{\alpha=v,c}\beta_{\alpha\mathbf{k}_0}(t)\Phi_{\alpha\mathbf{k}_0}^{(H)}(\mathbf{r},t). \tag{11}$$

The spatially varying periodic potential, $\Delta(y)$, couples different states in the y direction within each single band (CB or VB). As a result, the expansion coefficients in Eq. (11) satisfy the following system of differential equations:

$$\begin{aligned} i\hbar\frac{d\beta_{\mathbf{k}_0}^{(\mathrm{c})}}{dt} &= \mathbf{F}(t)\mathbf{Z}_{\mathbf{k}_0}(t)\beta_{\mathbf{k}_0}^{(\mathrm{v})} + \sum_{n=-\infty}^{\infty}\mathrm{V}_0\Lambda_{\mathbf{k}_0,\mathbf{k}_0+n\mathbf{Q}}^{(\mathrm{c},\mathrm{c})}\beta_{\mathbf{k}_0+n\mathbf{Q}}^{(\mathrm{c})} \\ &\quad + \sum_{n=-\infty}^{\infty}\mathrm{V}_0\Lambda_{\mathbf{k}_0,\mathbf{k}_0+n\mathbf{Q}}^{(\mathrm{c},\mathrm{v})}\beta_{\mathbf{k}_0+n\mathbf{Q}}^{(\mathrm{v})} \end{aligned} \tag{12}$$

and

$$\begin{aligned} i\hbar\frac{d\beta_{\mathbf{k}_0}^{(\mathrm{v})}}{dt} &= \mathbf{F}(t)\mathbf{Z}_{\mathbf{k}_0}^*(t)\beta_{\mathbf{k}_0}^{(\mathrm{c})} + \sum_{n=-\infty}^{\infty}\mathrm{V}_0\Lambda_{\mathbf{k}_0,\mathbf{k}_0+n\mathbf{Q}}^{(\mathrm{v},\mathrm{v})}\beta_{\mathbf{k}_0+n\mathbf{Q}}^{(\mathrm{v})} \\ &\quad + \sum_{n=-\infty}^{\infty}\mathrm{V}_0\Lambda_{\mathbf{k}_0,\mathbf{k}_0+n\mathbf{Q}}^{(\mathrm{v},\mathrm{c})}\beta_{\mathbf{k}_0+n\mathbf{Q}}^{(\mathrm{c})}, \end{aligned} \tag{13}$$

where we have used Fourier transformation to calculate the contributions of periodic gating.

Assuming potential $\Delta(y)$ to be smooth and weak enough, we will only take into account the first-order diffraction, $n = \pm1$. This is illustrated by the three coupled trajectories in Fig. 1. Hence, the above set of equations is simplified to

$$\begin{aligned} i\hbar\frac{d\beta_{\mathbf{k}_0}^{(\mathrm{c})}}{dt} &= \mathbf{F}(t)\mathbf{Z}_{\mathbf{k}_0}(t)\beta_{\mathbf{k}_0}^{(\mathrm{v})} \\ &\quad + \mathrm{V}_0\Lambda_{+}^{(\mathrm{c},\mathrm{c})}\beta_{\mathbf{k}_0+Q_y}^{(\mathrm{c})} + \mathrm{V}_0\Lambda_{+}^{(\mathrm{c},\mathrm{v})}\beta_{\mathbf{k}_0+Q_y}^{(v)} \\ &\quad + \mathrm{V}_0\Lambda_{-}^{(\mathrm{c},\mathrm{c})}\beta_{\mathbf{k}_0-Q_y}^{(\mathrm{c})} + \mathrm{V}_0\Lambda_{-}^{(\mathrm{c},\mathrm{v})}\beta_{\mathbf{k}_0-Q_y}^{(v)} \end{aligned} \tag{14}$$

and

$$\begin{aligned} i\hbar\frac{d\beta_{\mathbf{k}_0}^{(\mathrm{v})}}{dt} &= \mathbf{F}(t)\mathbf{Z}_{\mathbf{k}_0}^*(t)\beta_{\mathbf{k}_0}^{(\mathrm{c})} \\ &\quad + \mathrm{V}_0\Lambda_{+}^{(\mathrm{v},\mathrm{v})}\beta_{\mathbf{k}_0+Q_y}^{(\mathrm{v})} + \mathrm{V}_0\Lambda_{+}^{(\mathrm{v},\mathrm{c})}\beta_{\mathbf{k}_0+Q_y}^{(c)} \\ &\quad + \mathrm{V}_0\Lambda_{-}^{(\mathrm{v},\mathrm{v})}\beta_{\mathbf{k}_0-Q_y}^{(\mathrm{v})} + \mathrm{V}_0\Lambda_{-}^{(\mathrm{v},\mathrm{c})}\beta_{\mathbf{k}_0-Q_y}^{(c)}, \end{aligned} \tag{15}$$

with $\Lambda_{\lambda}^{(m,n)} = \langle \mathrm{m},\mathbf{k}_0|\mathrm{n},\mathbf{k}_0 \pm Q_y\rangle$, and indices m and n toggle between CB (c) and VB (v). Taking Eqs. (8) and (9) into account, explicit expressions for the coupling terms are

$$\Lambda^{(c,c)} = \Lambda^{(v,v)} = \cos\left(\varphi_{\mathbf{k}_0} - \varphi_{\mathbf{k}_0\pm Q_y}\right)/2 \tag{16}$$

and

$$\Lambda^{(c,v)} = \Lambda^{(v,c)*} = -i\sin\left(\varphi_{\mathbf{k}_0} - \varphi_{\mathbf{k}_0\pm Q_y}\right)/2. \tag{17}$$

The vector function, $\mathbf{Z}_{\mathbf{k}_0}(t)$, is proportional to the in-plane interband dipole matrix element,

$$\begin{aligned} \mathbf{Z}_{\mathbf{k}_0}(t) &= \mathbf{D}[\mathbf{k}_T(\mathbf{k}_0,t)] \\ &\quad \times e^{-\frac{i}{\hbar}\int_{-\infty}^{t}dt'\{E_c[\mathbf{k}_T(\mathbf{k}_0,t')] - E_v[\mathbf{k}_T(\mathbf{k}_0,t')]\}}. \end{aligned} \tag{18}$$

$\mathbf{D}(\mathbf{k}) = \{D_x(\mathbf{k}), D_y(\mathbf{k})\}$ is the interband dipole matrix element, which determines the coupling of the states of the CB and VB with wave vector $\mathbf{k}$ in the external electric field and is equal to

$$\mathbf{D}(\mathbf{k}) = \langle c, \mathbf{k}|e\mathbf{r}|v, \mathbf{k}\rangle. \tag{19}$$

Substituting the CB and VB wave functions (8) and (9) into Eq. (19), we obtain

$$D_x(\mathbf{k}) = \frac{ea}{2\sqrt{3}} \frac{1 + \cos\left(\frac{k_y a}{2}\right)\left[\cos\left(\frac{\sqrt{3}k_x a}{2}\right) - 2\cos\left(\frac{k_y a}{2}\right)\right]}{1 + 4\cos\left(\frac{k_y a}{2}\right)\left[\cos\left(\frac{\sqrt{3}k_x a}{2}\right) + \cos\left(\frac{k_y a}{2}\right)\right]} \tag{20}$$

and

$$D_y(\mathbf{k}) = \frac{ea}{2} \frac{\sin\left(\frac{k_y a}{2}\right)\sin\left(\frac{\sqrt{3}k_x a}{2}\right)}{1 + 4\cos\left(\frac{k_y a}{2}\right)\left[\cos\left(\frac{\sqrt{3}k_x a}{2}\right) + \cos\left(\frac{k_y a}{2}\right)\right]}. \tag{21}$$

The system of equations (14)-(15) describes the interband electron dynamics and determines the mixing of the CB and the VB states in the electric field of the pulse. Employing the appropriate initial condition, the time-dependent excitation probability and the CB population distribution, $N_c(\mathbf{k}_0, t) = |\beta^{(c)}_{\mathbf{k}_0}(t)|^2$, is calculated.

III. MAIN RESULTS

To introduce our idea, we turn to Fig. 1. The band structure, including the highest valence band (VB) and the lowest conduction band (CB) and showing the Dirac K and K' points, is presented in panel (a). The geometry of the system in the real space is displayed in panel (b) where a graphene monolayer is superimposed on a periodic array of nanowires under electrostatic bias, which periodically modulates the electron potential. Panel (c) shows an electron trajectory (the dashed red line) for an isolated monolayer of graphene in the reciprocal space caused by a single-oscillation circularly polarized pulse.

Those initial points for which the corresponding trajectories pass precisely through the Dirac point constitute a curve that is called separatrix (shown by the solid blue line) [10]. The separatrix is, in fact, a mirror reflection in the x axis of the electron trajectory originating at the K point. If the initial point, $\mathbf{k}_0$, is outside of the separatrix, as in panel (c), then the trajectory does not encircle the Dirac point, and the total Berry phase accumulated on such a trajectory is zero. In contrast, if $\mathbf{k}_0$ is inside the separatrix, as in panel (d), then the trajectory does encircle the Dirac point and, consequently, the Berry phase is $\pm\pi$ for the K and K' points, respectively.

Electron trajectories for graphene on a nanowire superlattice are illustrated in Fig. 1(e). The red line shows the actual electron trajectory in the reciprocal space staring at a crystal momentum $\mathbf{k}_0$, where the solid line corresponds to the electron in the VB and the dashed line to the electron in the CB. There are also two additional trajectories shown by the dash-dot blue and green lines that are obtained from the original (red) trajectory by shifting it by the superlattice reciprocal vectors, $\pm\mathbf{Q}$. The electron moving along the original (red) trajectory undergoes a Bragg reflection from the superlattice acquiring the wave vector $-\mathbf{Q}$ and jumping to the blue trajectory, as shown by a vertical arrow. This jump is necessarily accompanied by a VB $\rightarrow$ CB transition to avoid the Pauli blocking due to the VB being fully occupied. Passing by the K point, the electron undergoes the CB $\rightarrow$ VB transition and then another VB $\rightarrow$ CB transition at the point of the second Bragg reflection. The electron completes its trajectory at the initial $\mathbf{k}_0$ point but in the CB state. Note that, as can be understood, the transitions "across" (i.e., close to) the K point (between the red and blue trajectories in this case) are favored by the pseudospin selection rules [37] in comparison to transitions away from the K point (between the red and green trajectories, not shown). We show in panel (e) only such favored transitions, which also are enhanced due to an increase of the interband dipole matrix element in the vicinity of the K point.

Analogous arguments are applicable to the alternative case when the $\mathbf{k}_0$ point is inside the separatrix shown in Fig. 1(f). However, in this case the transitions across the K point, which are enhanced, are those between the original red trajectory and the Bragg-shifted green trajectory.

In both cases of the initial crystal moments inside and outside of the separatrix [Fig. 1(e) and 1(f)], the electron circles around the K point, but only part of its trajectory. Therefore the Berry phase, ϕ, accumulated due to such a passage is reduced with respect to the complete circling: $|\phi| < \pi$. (Note that the jumps due to the Bragg reflections do not contribute to the Berry phase.) Thus in a self-referenced interferometry, the phase will be observable since $2|\phi| < 2\pi$.

Fundamentally, the CB population induced by the strong optical field is measurable in the reciprocal space by time- and angle-resolved photoemission spectroscopy (TR-ARPES) techniques [14,38–40]. Resolving the electrons originating from the CB after the pulse ends but before the electron collisions smear out the distribution, one will register a self-referenced interferogram. Because $2|\phi| < 2\pi$, there will be discontinuities of the electron distribution on all three separatrices shown in Figs. 1(e) and 1(f).

Consider first the results obtained for a single-oscillation circularly polarized optical pulse illustrated in Fig. 1. These are shown in Fig. 2 where the electron population of the conduction band, $N_c(\mathbf{k}, t)$, is displayed in the reciprocal space after the end of the excitation pulse whose amplitude is $F_0 = 0.5$ V/Å. As one can see, the distributions of the population in the vicinity of the K vs K' point are different because the chirality of the circularly polarized pulse causes significantly different electron trajectories at the nonequivalent Dirac points, which are intrinsically chiral themselves. (Note that for linearly polarized pulses, there is no such a distinction: the distributions at the K and K' points are identical [35].) As expected [see Figs. 1(e) and 1(f) and the related discussion], there are discontinuities at the positions of all three separatrices due to the partial Berry phase $2|\phi| < 2\pi$.

To elucidate the phases of the electronic states in the presence of the topological $\pm\pi$ Berry fluxes at the Dirac points, we will use the idea of self-referenced interferometry in the reciprocal space [10]. Consider a pulse with two oscillations of opposite circularities, as shown in the inset of Fig. 3. The idea is that during such a pulse, an electron, which moves in the reciprocal space according to Eq. (1), passes twice, in the opposite directions, in the vicinity of the Dirac point

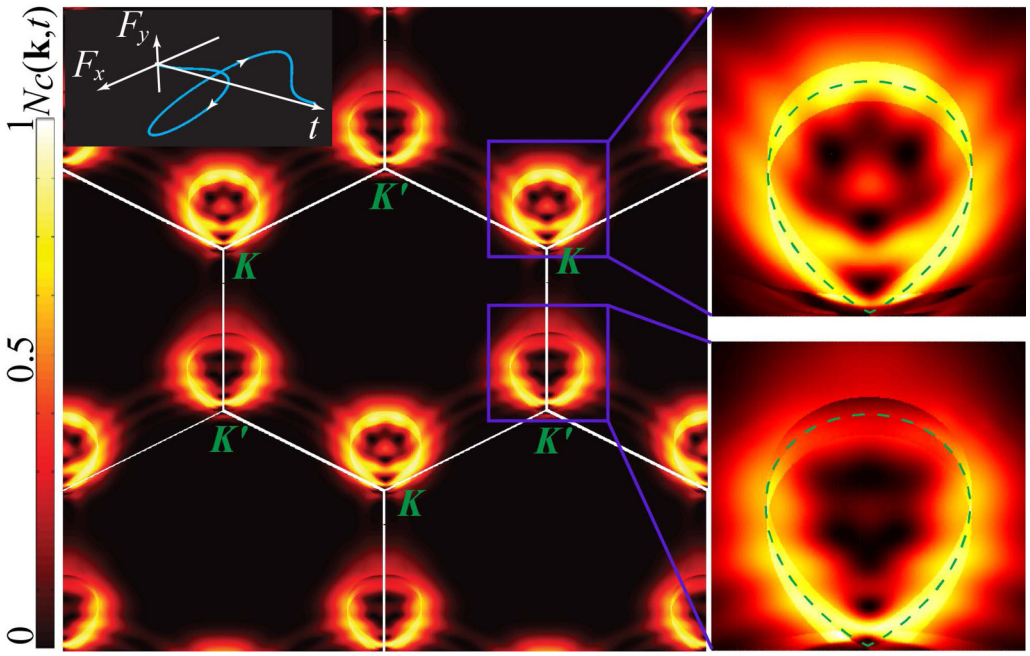

FIG. 2. Conduction band population $N_c(\mathbf{k},t)$ in the reciprocal space in the extended Brillouin zone picture plotted (color coded) as a function of crystal momentum $\mathbf{k}$ at time t at the end of the optical pulse. The pulse has one optical oscillation with a circular polarization, duration of 5 fs, and amplitude of $F_0 = 0.5$ V/Å, as shown in the inset. Magnified distributions around the two nonequivalent Dirac points, K and K', are shown in the right panels. The separatrix is indicated by the dashed green line superimposed on the population distribution. The three discontinuities are clearly seen at the separatrix and its replicas Bragg-shifted by $\pm\mathbf{Q}$.

where the VB $\leftrightarrow$ CB transitions are likely to occur. After the pulse, the electron crystal momentum returns back to its initial value $\mathbf{k}_0$ irrespectively of the quantum transitions that have occurred. Consequently, the amplitudes corresponding to the VB $\leftrightarrow$ CB transitions during these two passes interfere. Their phases differ by a dynamic phase, which is due to the energy difference between the VB and the CB and leads to formation of interference fringes, and the Berry phase of 2ϕ. In pure

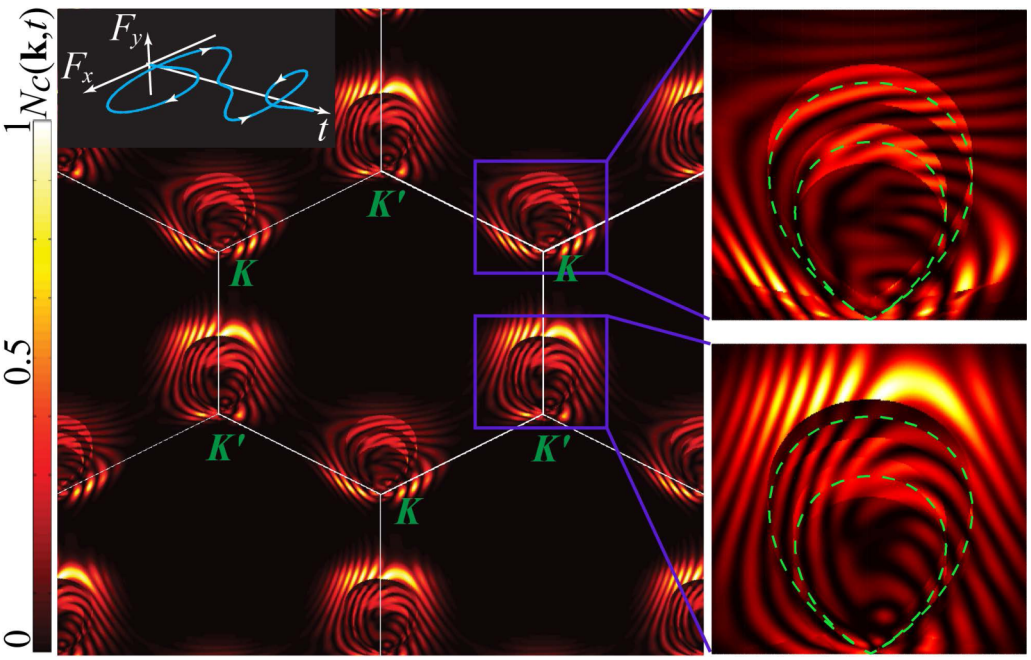

FIG. 3. Similar to Fig. 2 but with a two-cycle pulse with opposite circularities (clockwise then counterclockwise) for the two periods. The field amplitude ratio for the first and second periods is $\alpha = 0.75$. The expanded images of CB population near the K and K' points are shown on the separate panels to the right. The two separatrices corresponding to the two optical-oscillation periods are indicated by the dashed green lines.

graphene, the Berry phase $\phi = \pm\pi$; this results in the phase of $2\phi = \pm 2\pi$ in the self-referenced interferometry. Thus the Berry phase does not lead to discontinuities of the electron population fringes. In our case of a superlattice, $|2\phi| < 2\pi$, and there will be both intensity discontinuities and fringe shifts on the separatrices and their Bragg images.

The resulting momentum distribution of electrons at the end of the two-oscillation chiral pulse is shown in Fig. 3. It is an interferogram with many interference fringes, which is highly chiral in the vicinity of the Dirac points. There are bifurcations of fringes clearly present at the interferogram, which are characteristic of vertices.

Interestingly enough, the number and density of fringes at the K' point is appreciably greater than at the K point. In fact, in one case, the Berry phase adds to the dynamic phase; in a pure graphene, the addition of the $2\phi = 2\pi$ geometric phase to the self-referenced interferogram causes an appearance of an extra fringe. In the other case, it subtracts from the dynamic phase, which causes the disappearance of one fringe. An important peculiarity of these interferograms is their singularity: there are both amplitude discontinuities and fringe shifts at the two separatrices (corresponding to the two optical periods) and their Bragg replicas. From the more general point of view, the electron interferograms of the predicted type contain information on such important topological characteristic as the Berry curvature in the reciprocal space.

To better visualize the jump in CB population amplitude, we plot the CB population probability distribution along a vertical line in reciprocal space; i.e., for a fixed value of q_x we draw $N_c(\mathbf{k},t) = |\beta^{(c)}_{\mathbf{k}}(t)|^2$ with respect to q_y in Fig. 4. Panel (a) corresponds to the one-cycle pulse, whereas panel (b) is related to a two-cycle field.

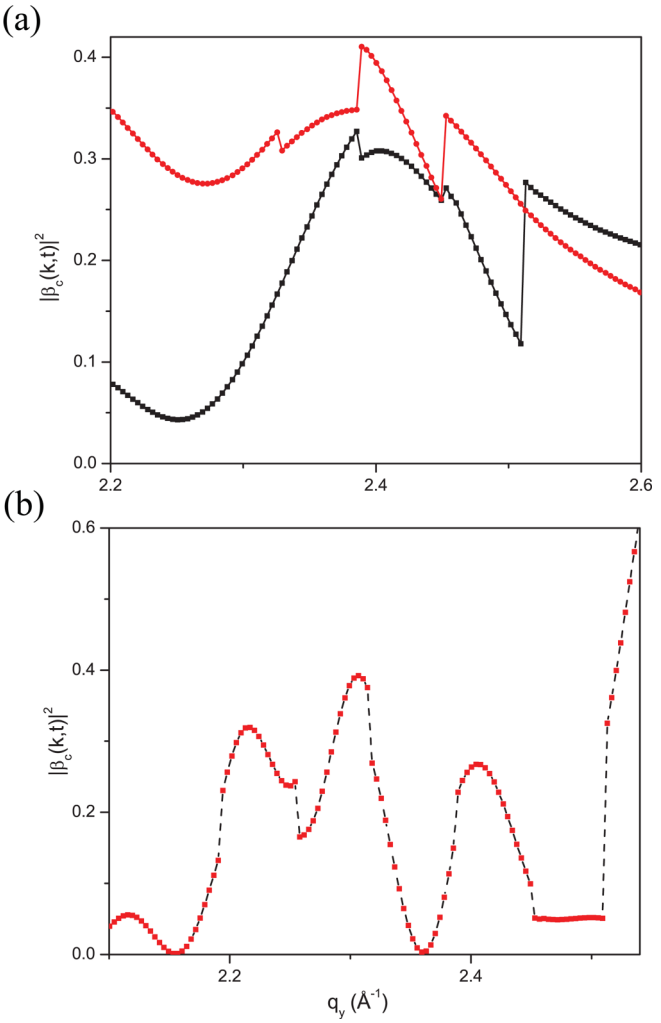

FIG. 4. Residual CB population plotted as a function of q_y with a fixed value of q_x. Panel (a) corresponds to a one-cycle pulse (Fig. 2) with $q_x = 0.1$ Å^{-1} (black) and $q_x = 0.2$ Å^{-1} (red). The three jumps stemming from the nontrivial geometric (Berry) phase are evident. Panel (b) corresponds to a two-cycle pulse (Fig. 3) with the second cycle of the opposite rotation and an amplitude ratio of $\alpha = 0.75$. For this plot, $q_x = 0.1$ Å^{-1}. There are six jumps visible originating from the nontrivial Berry phase.

IV. DISCUSSION

Lets us briefly discuss our results and approaches to observe experimentally the phenomena predicted.

As we have already mentioned above in the introductory part of this paper, the interferograms of Figs. 2 and 3 can be read out using TR-ARPES, where an extreme ultraviolet (XUV) pulse transfers the graphene electrons into the continuum. These electrons are analyzed in their energy and tangential momentum. The XUV pulse should have energy uncertainty less than the VB $\leftrightarrow$ CB transition energy, which is needed to resolve the CB- from VB-originating electrons. Given that the shortest known electron-momentum relaxation times in graphene are $\tau_e \gtrsim 10$ fs, the corresponding energy width of the XUV pulse in TR-ARPES should be $\Delta E \sim \hbar/\tau_e \lesssim 0.1$ eV, which will allow one to resolve the CB electrons for most of the interferograms in Figs. 2 and 3.

The electron-electron collision dynamics will manifest itself by the smearing-out of the interferograms, which can also be traced by TR-ARPES with a temporal resolutions of a few fs and the momentum resolution defined by the ARPES setup, which is realistically ~1.5 percent of the Brillouin zone edge ($\approx$1.6 Å^{-1}), that is $\approx$0.025 Å^{-1} [38]; the momentum resolution can be as high as 0.005 Å^{-1} for nano-ARPES [41]. Such resolutions are more than sufficient to observe the interference fringes predicted in this paper and their evolution caused by electron collisions. Note that TR-ARPES with XUV energy and requirements close to the energy and momentum resolution has recently been used to resolve $\lesssim$100 as lifetimes in highly excited bands of a solid [40].

V. CONCLUSIONS

In conclusion, we have proposed an approach to observe the direct manifestations of the topological nature of graphene in the conduction band population distribution. We previously showed that graphene interacting with an ultrafast circularly polarized pulse acts as an attosecond interferometer with self-referencing capabilities [10]. The topological nature of graphene's reciprocal space leads to appearance of the $\pm\pi$ Berry phase for electrons circling around a Dirac point. However, directly observing such a phase as discontinuities in

the electron CB distribution in native graphene is impossible since such distributions are self-referenced interferograms. Consequently, the relevant phase is twice the Berry phase, $\pm 2\pi$, which eliminates the interferograms' discontinuities.

In this article we have proposed to use graphene on an underlying periodic superlattice with a relatively large period. Due to the electron Bragg reflections from this superlattice, the circling around the Dirac point becomes incomplete and the accumulated phase not equal to $\pm 2\pi$, which does lead to the characteristic discontinuities of the electron CB distribution at the separatrices. This directly visualizes the topological curvature and Berry fluxes of the graphene reciprocal space.

From the point of view of fundamental symmetries, graphene possesses mirror ($\mathcal{P}$) symmetry with respect to reflection in the xz plane and is invariant with respect to time reversal ($\mathcal{T}$ symmetric). These symmetries imply, in particular, that the K and K' points have the same properties except their Berry curvatures are opposite, leading to the opposite Berry phases of $\pm\pi$. Related to these symmetries is that the Chern number is zero, and graphene is globally topologically trivial. In a sharp contrast, the state in which a strong (non perturbative) ultrashort circularly polarized pulse leaves graphene does not have either $\mathcal{P}$ or $\mathcal{T}$ symmetry. It has the sense of rotation determined by the circular polarization of the excitation pulse and is fundamentally optically active. This and similar "topologically charged" states of matter created by intense, ultrafast, and chiral optical fields are of significant interest fundamentally and for applications in petahertz-bandwidth information processing. The dynamics that we predict is attosecond: over twenty fringes are formed during a 5 fs duration of the second of the two pulses. This implies attosecond dynamics: $\approx$200 as per fringe.

ACKNOWLEDGMENTS

This work was supported by Grant No. DE-FG02-01ER15213 from the Atomic, Molecular and Optical Sciences Program, Office of Basic Energy Sciences, the US Department of Energy. Theoretical work of V.A. was supported by Grant No. ECCS-1308473 from the National Science Foundation.

[1] D. J. Thouless, *Topological Quantum Numbers in Nonrelativistic Physics* (World Scientific, Singapore, 1998).
[2] J. M. Kosterlitz and D. J. Thouless, in *40 Years of Berezinskii-Kosterlitz-Thouless Theory* (World Scientific, Singapore, 2013), pp. 1–67.
[3] M. Z. Hasan and C. L. Kane, Rev. Mod. Phys. **82**, 3045 (2010).
[4] M. V. Berry, Proc. R. Soc. London Ser. A **392**, 45 (1984).
[5] L. Duca, T. Li, M. Reitter, I. Bloch, M. Schleier-Smith, and U. Schneider, Science **347**, 288 (2015).
[6] W. Ehrenberg and R. E. Siday, Proc. Phys. Soc. Sect. B **62**, 8 (1949).
[7] Y. Aharonov and D. Bohm, Phys. Rev. **115**, 485 (1959).
[8] R. G. Chambers, Phys. Rev. Lett. **5**, 3 (1960).
[9] F. Bloch, Z. Phys. A **52**, 555 (1929).
[10] H. K. Kelardeh, V. Apalkov, and M. I. Stockman, Phys. Rev. B **93**, 155434 (2016).
[11] N. Flaschner, B. S. Rem, M. Tarnowski, D. Vogel, D. S. Luhmann, K. Sengstock, and C. Weitenberg, Science **352**, 1091 (2016).
[12] G. P. Thomson, Science **70**, 541 (1929).
[13] C. Hwang, C. H. Park, D. A. Siegel, A. V. Fedorov, S. G. Louie, and A. Lanzara, Phys. Rev. B **84**, 125422 (2011).
[14] Y. Liu, G. Bian, T. Miller, and T. C. Chiang, Phys. Rev. Lett. **107**, 166803 (2011).
[15] M. Gmitra, S. Konschuh, C. Ertler, C. Ambrosch-Draxl, and J. Fabian, Phys. Rev. B **80**, 235431 (2009).
[16] D. Pesin and A. H. MacDonald, Nat. Mater. **11**, 409 (2012).
[17] J. Moore, Nat. Phys. **5**, 378 (2009).
[18] J. E. Moore, Nature (London) **464**, 194 (2010).
[19] X.-L. Qi and S.-C. Zhang, Phys. Today **63** (1), 33 (2010).
[20] D. Hsieh, Y. Xia, D. Qian, L. Wray, F. Meier, J. H. Dil, J. Osterwalder, L. Patthey, A. V. Fedorov, H. Lin, A. Bansil, D. Grauer, Y. S. Hor, R. J. Cava, and M. Z. Hasan, Phys. Rev. Lett. **103**, 146401 (2009).
[21] T. Zhang, P. Cheng, X. Chen, J.-F. Jia, X. Ma, K. He, L. Wang, H. Zhang, X. Dai, Z. Fang, X. Xie, and Q.-K. Xue, Phys. Rev. Lett. **103**, 266803 (2009).
[22] Y. Sakamoto, T. Hirahara, H. Miyazaki, S.-I. Kimura, and S. Hasegawa, Phys. Rev. B **81**, 165432 (2010).
[23] J. G. Analytis, J.-H. Chu, Y. Chen, F. Corredor, R. D. McDonald, Z. X. Shen, and I. R. Fisher, Phys. Rev. B **81**, 205407 (2010).
[24] T. Hirahara, Y. Sakamoto, Y. Takeichi, H. Miyazaki, S.-I. Kimura, I. Matsuda, A. Kakizaki, and S. Hasegawa, Phys. Rev. B **82**, 155309 (2010).
[25] S. A. O. Motlagh, V. Apalkov, and M. I. Stockman, Phys. Rev. B **95**, 085438 (2017).
[26] M. Breusing, S. Kuehn, T. Winzer, E. Malic, F. Milde, N. Severin, J. P. Rabe, C. Ropers, A. Knorr, and T. Elsaesser, Phys. Rev. B **83**, 153410 (2011).
[27] K. J. Tielrooij, J. C. W. Song, S. A. Jensen, A. Centeno, A. Pesquera, A. Zurutuza Elorza, M. Bonn, L. S. Levitov, and F. H. L. Koppens, Nat. Phys. **9**, 248 (2013).
[28] D. Brida, A. Tomadin, C. Manzoni, Y. J. Kim, A. Lombardo, S. Milana, R. R. Nair, K. S. Novoselov, A. C. Ferrari, G. Cerullo, and M. Polini, Nat. Commun. **4**, 1987 (2013).
[29] I. Gierz, J. C. Petersen, M. Mitrano, C. Cacho, I. C. Turcu, E. Springate, A. Stohr, A. Kohler, U. Starke, and A. Cavalleri, Nat. Mater. **12**, 1119 (2013).
[30] M. W. Graham, S.-F. Shi, D. C. Ralph, J. Park, and P. L. McEuen, Nat. Phys. **9**, 103 (2013).
[31] J. C. Johannsen, S. Ulstrup, F. Cilento, A. Crepaldi, M. Zacchigna, C. Cacho, I. C. E. Turcu, E. Springate, F. Fromm, C. Raidel, T. Seyller, F. Parmigiani, M. Grioni, and P. Hofmann, Phys. Rev. Lett. **111**, 027403 (2013).
[32] I. Gierz, F. Calegari, S. Aeschlimann, M. C. Cervantes, C. Cacho, R. T. Chapman, E. Springate, S. Link, U. Starke, C. R. Ast, and A. Cavalleri, Phys. Rev. Lett. **115**, 086803 (2015).
[33] J. C. Johannsen, S. Ulstrup, A. Crepaldi, F. Cilento, M. Zacchigna, J. A. Miwa, C. Cacho, R. T. Chapman, E. Springate,

F. Fromm, C. Raidel, T. Seyller, P. D. C. King, F. Parmigiani, M. Grioni, and P. Hofmann, Nano Lett. **15**, 326 (2015).
[34] W. V. Houston, Phys. Rev. **57**, 184 (1940).
[35] H. K. Kelardeh, V. Apalkov, and M. I. Stockman, Phys. Rev. B **91**, 045439 (2015).
[36] H. K. Kelardeh, V. Apalkov, and M. I. Stockman, Phys. Rev. B **92**, 045413 (2015).
[37] A. H. C. Neto, F. Guinea, N. M. R. Peres, K. S. Novoselov, and A. K. Geim, Rev. Mod. Phys. **81**, 109 (2009).
[38] A. Damascelli, Z. Hussain, and Z.-X. Shen, Rev. Mod. Phys. **75**, 473 (2003).
[39] I. Gierz, M. Lindroos, H. Hochst, C. R. Ast, and K. Kern, Nano Lett. **12**, 3900 (2012).
[40] Z. Tao, C. Chen, T. Szilvsi, M. Keller, M. Mavrikakis, H. Kapteyn, and M. Murnane, Science **353**, 62 (2016).
[41] J. Avila, I. Razado, S. Lorcy, R. Fleurier, E. Pichonat, D. Vignaud, X. Wallart, and M. C. Asensio, Sci. Rep. **3**, 2439 (2013).